ACS Photonics

Letter

Cite This: ACS Photonics 2019, 6, 830−837

pubs.acs.org/journal/apchd5

Optically Modulated Ultra-Broadband All-Silicon Metamaterial Terahertz Absorbers

Xiaoguang Zhao,[†,‡] Yue Wang,[†,§] Jacob Schalch,[∥] Guangwu Duan,[‡] Kevin Cremin,[∥] Jingdi Zhang,[∥] Chunxu Chen,[‡] Richard D. Averitt,[*,∥] and Xin Zhang[*,‡]

[‡]Department of Mechanical Engineering, Boston University, 110 Cummington Mall, Boston, Massachusetts 02215, United States
[§]Department of Applied Physics, Xi'an University of Technology, South Jinhua Road, Xi'an, Shaanxi 710048, China
[∥]Department of Physics, University of California, San Diego, 9500 Gilman Dr., La Jolla, California 92093, United States

Supporting Information

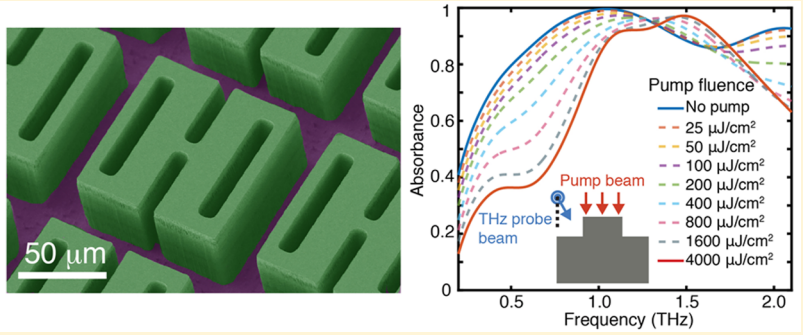

ABSTRACT: Terahertz perfect absorbers represent an essential photonic component for detecting, modulating, and manipulating terahertz radiation. We utilize single-layer H-shaped all-silicon arrays to demonstrate tunable ultra-broadband terahertz wave absorption. Experiment and simulation reveal near unity absorption at 1 THz, with a bandwidth of ∼913 GHz for ≥90% absorbance. The absorption is optically tunable, exhibiting a resonance frequency blueshift by 420 GHz, while the peak absorbance remains over 99%. The dynamic response upon optical excitation depends on the penetration depth of the pump beam in silicon, as demonstrated through simulations that take into account the depth dependence of the carrier concentration in the all-silicon metamaterial perfect absorber. Notably, our all-silicon and ultrabroadband metamaterial perfect absorber is compatible with CMOS processing, potentially facilitating the development of terahertz detectors. Furthermore, the demonstrated tunable response may find potential applications toward creating dynamic functional terahertz devices, such as modulators and switches.

KEYWORDS: *metamaterial perfect absorber, all-silicon, ultra-broadband, terahertz absorber, optical modulation*

Terahertz (THz) technologies, referring the frequency ranging from 0.1 THz to 10 THz, potentially enable a wide range of applications, including wireless communication,[1] biochemical sensing,[2] and nondestructive imaging.[3] One major research direction is to construct compact and practical THz systems, which depends on the development of miniaturized components such as sources, detectors, modulators, switches and absorbers. Advances in electromagnetic metamaterials[4] have greatly improved our capabilities to manipulate THz waves, which provides significant opportunities toward constructing practical THz devices.

Over the past decade, in particular, THz metamaterial perfect absorbers (MPAs) have attracted great interest due to their potential applications in physics, medicine, material science, and chemistry.[5] Previous reports were mainly focused on single-frequency[6−8] and multiple-band[9−11] THz absorbers based on sandwiched layers of metallic resonators/dielectric spacer/metal ground plane. Recently, all-dielectric[12,13] and all metal[14] THz absorbers have been developed to construct the MPAs using a single material with three-dimensional geometries. One hurdle toward utilizing MPAs in some applications, such as THz detection and imaging, is the narrow bandwidth. Even though MPAs with a tunable response may extend the absorption bandwidth,[15−17] an absorber that simultaneously absorbs across a broad bandwidth is desirable.

Recently, broadband THz absorbers have been widely investigated for various applications.[18−25] One realization of MPAs is through judicious stacking of several resonant layers.[18,19] However, the fabrication inevitably involves multilayer thin film deposition, which is too complicated to meet the requirement of practical integration in modern thin, planar THz devices. All-dielectric broadband absorbers provide another approach. Notably, at infrared frequencies, all-silicon

Received: November 27, 2018
Published: January 25, 2019

DOI: 10.1021/acsphotonics.8b01644
ACS Photonics 2019, 6, 830−837

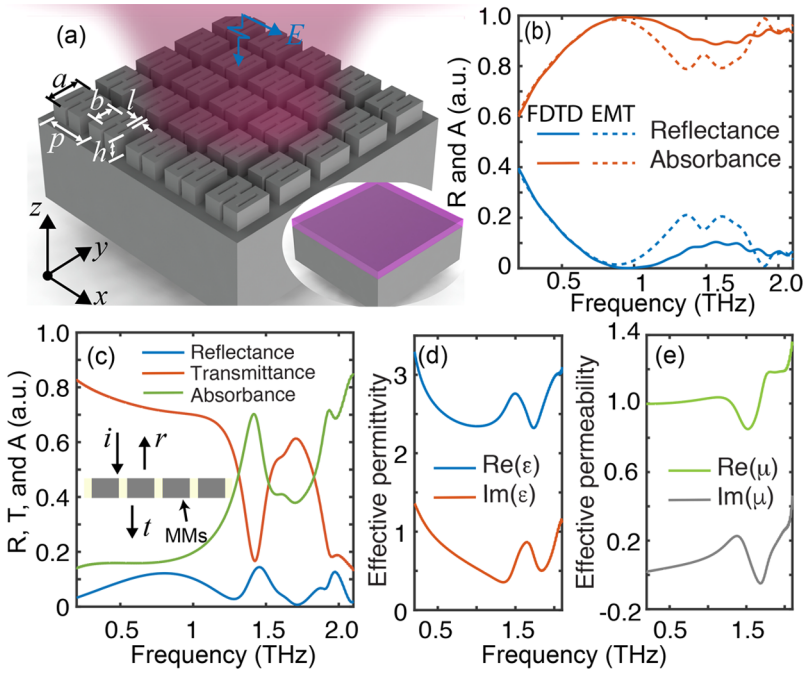

Figure 1. (a) Schematic of all-dielectric broadband THz metamaterial perfect absorber. For the H-shaped unit cell, the periodicity is p = 140 μm, side-width a = 110 μm, thickness of the MM layer h = 53 μm. For the holes in the bars of the H-shaped unit cell, the width of the hole is b = 82 μm, and the length of the hole is l = 12 μm. Inset: Effective medium theory model of the MPA, in which the MM layer is considered as a homogeneous thin film. (b) FDTD simulated reflectance and absorbance of a MPA structure and corresponding calculated spectrum using effective medium theory (EMT). In the FDTD simulation, more than 90% absorbance is achieved from 0.59 THz to 1.49 THz. (c) Simulated reflectance, transmittance, and absorbance of free-standing MM layer for effective parameter extraction. (d) and (e) are the effective permittivity and permeability extracted from the spectrum of the MM layer (c): R, reflectance; T, transmittance; and A, absorbance.

structures have been employed as broadband perfect absorbers.[26−29] Similar broadband perfect absorbers can be employed for THz applications. For example, disordered silicon metamaterials[20] and double layered gratings[23] have been employed to construct broadband perfect absorbers, but these structures require sophisticated design and fabrication of the silicon structures. Meanwhile, the optical tunability and nonlinearities that have been explored in narrow band all-dielectric absorbers,[30,31] have not been fully investigated for broadband MPAs.

In this paper, we present an all-silicon MPA, consisting of a single-layer of uniformly distributed "H-shaped" metamaterials patterned on a silicon substrate. In addition to static characterization, we investigate the dynamic response under optical excitation. In measurements of the static state, the MPA exhibits near-perfect absorption at 1 THz and a 90% absorbance bandwidth of 0.9 THz. We employ the effective medium theory and finite difference time domain simulations to analyze the physics of the perfect absorption and attribute the broadband response to the overlap of different resonant modes. Excitation with ∼100 fs 800 nm pulses results in a resonance mode shift and modulation of the bandwidth and absorbance as the pump fluence increases from 0 to 4000 μJ/cm^2. The results can be explained using multilayer carrier dynamics in the metamaterial structure arising from the pump light penetration depth. Our work demonstrates using single-layer all-dielectric metamaterials to construct a MPA for CMOS-compatible THz detection and imaging. In addition, the optically tunable response demonstrates flexibility to manipulate THz waves for potential applications as modulators and switches.

RESULTS AND DISCUSSION

Design and Effective Medium Theory. The THz absorber design is illustrated in Figure 1a, consisting of a metamaterial (MM) layer on a silicon substrate. The unit cell of the MM layer is a H-shaped microstructure with two rectangular cavities on each side bar, that are deeply etched into the silicon wafer, which is p-type boron doped with a carrier density of 3.0 × 10^{16} cm^{-3}. The overall thickness of the wafer is 300 μm and the thickness of the MM layer is designed as 50 μm. Details of the geometrical parameters can be found in Figure S1 of the Supporting Information. The cavities in the side bars of the H-shaped unit cell are designed to increase the absorption bandwidth, as shown in Figure S2 in the Supporting Information. In order to design and optimize the structure of the MPA, we obtain the reflectance (R) and transmittance (T) of MPAs with different geometries using finite difference time domain (FDTD) simulations and calculate the absorbance (A) with the equation $A = 1 - R - T$. Figure 1b is the simulated spectra of a MPA design with the geometry listed in Table S1 in the Supporting Information. In the simulation, the permittivity of silicon is modeled with a Drude response and the polarization of the incident terahertz pulses is along the x-axis, as shown in Figure 1a and as detailed in the Methods section. The simulation results reveal that near unity absorbance is achieved at 1 THz and a bandwidth for 90% absorbance of approximately 900 GHz, yielding a broadband perfect absorber. The perfect absorption frequency is highly related to the thickness of the MM structure. That is, the thicker (thinner) MM layers result in lower (higher) perfect absorption frequencies, as illustrated by Figure S3 in the Supporting Information. The simulations demonstrate that it

DOI: 10.1021/acsphotonics.8b01644
ACS Photonics 2019, 6, 830−837

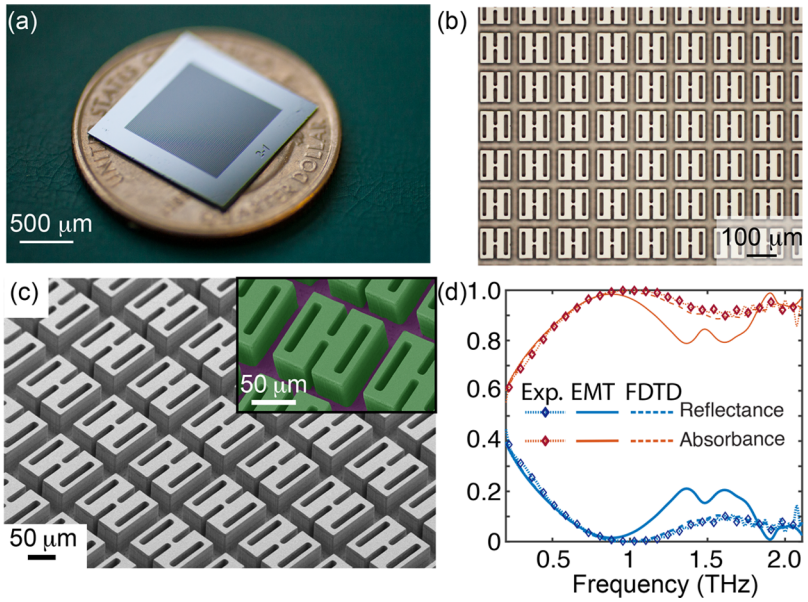

Figure 2. (a) Picture of the all-silicon MPA. The absorber area is 1 cm × 1 cm. (b) Optical microscope image of the MPA. (c) Scanning electron microscope (SEM) image of the all-silicon MPA. Inset: false color SEM view of the unit cell. The green part is the etched silicon and the purple part is the silicon substrate. (d) The reflectance and absorbance spectrum of the fabricated MPA, comparing EMT and FDTD with experiment.

should be possible to experimentally achieve broadband perfect absorption with an all-silicon MPA.

For our all-dielectric MPA, the MM unit cells are subwavelength. Thus, the MM layer can be treated as an effective medium with the same thickness on top of the silicon substrate. In order to extract the effective properties, we simulate the reflection and transmission response of a free-standing MM layer, identical to the MPA except without the silicon substrate as shown in Figure 1c. The MM layer exhibits sharp resonance at ∼1.4 THz with a transmission minimum value and local maximum value in reflection, which induces a narrow band absorption in the vicinity of the resonance frequency. This resonance corresponds to the transverse magnetic mode of the H-shaped resonator, as shown in Figure S4. The peak absorbance of the standalone MM layer is ∼0.7. Comparing to the all-silicon MPA with the silicon substrate (Figure 1b), the standalone MM layer absorbs less of the THz wave over a much narrower bandwidth. When a silicon substrate is introduced underneath the MM layer, multiple reflection arises inside the MM layer due to the existence of substrate, resulting in a broadband near-unity absorbance. In other words, the MM layer with its effective permittivity acts like a broadband antireflection coating on the silicon substrate. Meanwhile, the high imaginary refractive indices of the MM layer and silicon substrate absorb the incident wave. To verify this hypothesis, we first perform the parameter retrieval to extract the effective permittivity and permeability based on the transfer matrix method (TMM).[32] Details of the parameter retrieval may be found in the Methods section. The Drude model for the silicon has been tailored to exhibit dispersive effective permittivity and permeability, as shown in Figure 1d,e. At lower frequencies, the effective permittivity (both the real and imaginary part) is much smaller than bare silicon since much of the silicon has been removed, as illustrated by comparing Figure 1d and Figure S5 in the Supporting Information. In the vicinity of 1.42 THz, there is a peak in the effective permittivity associated with the resonance of the H-shaped unit cell. The effective permeability is close to one at low frequencies, similar to bare silicon, as there is no magnetic response in the structure. However, at higher frequencies, the permeability exhibits dispersion attributed to the bianisotropic response in the MMs.[33]

We use effective medium theory (EMT) to calculate the response of the all-dielectric MPA quantitatively. In the model, we use the retrieved effective parameters for the MM layer to calculate the reflection coefficient and transmission of the system including the substrate using the TMM.[34] The stacked (1/2/3/4) layers are configured as air/MM/Si/air. The reflection (r) and transmission (t) coefficient for normal incidence are

$$r = \frac{e^{-i\delta_3}(r_{1,2}e^{-i\delta_2} + r_{2,3}e^{i\delta_2}) + r_{3,4}e^{i\delta_3}(r_{1,2}r_{2,3}e^{-i\delta_2} + e^{i\delta_2})}{e^{-i\delta_3}(e^{-i\delta_2} + r_{1,2}r_{2,3}e^{i\delta_2}) + r_{34}e^{i\delta_3}(r_{2,3}e^{-i\delta_2} + r_{1,2}e^{i\delta_2})} \quad (1)$$

$$t = \frac{t_{1,2}t_{2,3}t_{3,4}}{e^{-i\delta_3}(e^{-i\delta_2} + r_{1,2}r_{2,3}e^{i\delta_2}) + r_{3,4}e^{i\delta_3}(r_{2,3}e^{-i\delta_2} + r_{1,2}e^{i\delta_2})} \quad (2)$$

in which $r_{m,m+1}$ and $t_{m,m+1}$ are the reflection and transmission at the interface between layer m and $m + 1$, and $\delta_m = n_m k d_m$ is the phase delay in layer m, where n_m ($n_m = \sqrt{\varepsilon_m \mu_m}$) and d_m are the refractive index and thickness for layer m respectively, k is the wavenumber, and ε_m and μ_m are the relative permittivity and permeability of layer m, respectively. Based on the Fresnel equations, the reflection ($r_{m,m+1}$) and transmission ($t_{m,m+1}$) coefficient for waves propagating from layer m to layer $m + 1$ can be calculated by

$$r_{m,m+1} = \frac{n_m - n_{m+1}}{n_m + n_{m+1}} \quad (3)$$

$$t_{m,m+1} = \frac{2n_m}{n_m + n_{m+1}} \quad (4)$$

The refractive index of the MM layer is calculated using the effective permittivity and permeability, as shown in Figure 1d,e.

DOI: 10.1021/acsphotonics.8b01644
ACS Photonics 2019, 6, 830−837

The calculated spectrum based on EMT is plotted in Figure 1b, which agrees well with FDTD results. At low frequencies, EMT accurately captures the FDTD results, with slight deviation for frequencies above 1.1 THz. In particular, a weak absorption peak can be seen in the EMT mode in the vicinity of 1.5 THz, corresponding to the resonance frequency of the MM layer, which is absent in the FDTD simulation. It may be that the presence of the substrate dampens the resonance of the MM layer through near field coupling, which is neglected in the EMT model. The qualitative agreement between TMM calculation and FDTD validates EMT. Of course, EMT overlooks some details of the near field interactions, but nonetheless provides an overall macroscopic understanding of the MPA response. Therefore, in the all-dielectric MPA, the MM layer can be considered as a homogeneous material with effective properties that function as a broadband antireflection coating. At the same time, the large imaginary refractive indices in the MM layer and silicon substrate lead to high absorption of the incident THz radiation. In short, EMT is a generic model that can be applied not only to our specific case, but also to the design of other metamaterial based devices working at arbitrary frequencies.

Experimental Results of Broadband Absorption. In order to validate the all-dielectric MPA design experimentally, we fabricated a MPA sample using bulk micromachining processes and characterized the resultant device using THz time domain spectroscopy (TDS). We used photolithography and subsequent deep reactive ion etching (DRIE) to pattern silicon, forming the MM layer. The fabricated absorber is shown in Figure 2a and the metamaterial structure is shown in Figures 2b and 2c. The etching depth is approximately 53 μm and other geometries are the same as the designed value (see section S1 in the Supporting Information). The etching process is well controlled to avoid errors and defects in the fabrication.

The experimental reflectance and absorbance spectrum of the all-dielectric MPA is shown in Figure 2d. Details of the characterization can be found in the Methods section. The peak absorbance (~99.99%) occurs at 0.97 THz, with a bandwidth of ~900 GHz for 90% absorbance. In the vicinity of 2.0 THz, another resonance mode appears, leading to an increase in absorbance to 96%. The merger of two resonance modes broadens the absorbance bandwidth, resulting in broadband absorption. The FDTD simulation result matches the experimental spectrum over the entire spectrum range from 0.2 THz to 2.1 THz, which validates our numerical model. In order to understand the experimental results, we performed full-wave simulations to identify the resonance modes of the all-dielectric MPA as shown in Figure 3. The resonance modes correspond to waveguide modes, which are hybrid of magnetic (EH) and electric (HE) modes, similar to a narrow band all-dielectric perfect absorber.[13] An EH mode represents a hybrid mode in which the transverse magnetic (TM) mode dominates, whereas a HE mode represents a hybrid mode in which the transverse electric (TE) mode dominates.[35] Examining the field distribution at a resonance frequency permits identification of which mode (i.e., EH or HE) is being excited. The first and second column in Figure 3a,b demonstrate the electric and magnetic field distribution for 0.97 THz and 2.0 THz, respectively, to classify the resonance modes in the MPA. The lower frequency mode, as shown in the left two columns of Figure 3a, is dominated by the TE field

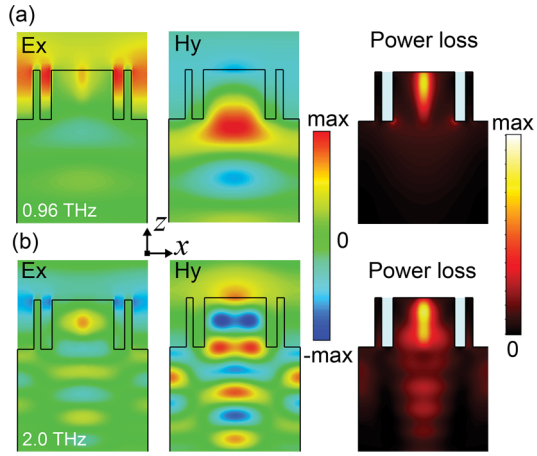

Figure 3. Electric (first column) and magnetic (second column) field distribution and power loss density (third column) for (a) 0.96 THz and (b) 2.0 THz resonance modes, respectively.

in the metamaterial layer, indicating a HE mode. The higher frequency mode is dominated by the transverse magnetic mode, indicating a EH mode, as shown in the left two columns of Figure 3b. The incident waves couples into the all-dielectric MPA structure with little reflection through these waveguide modes and is absorbed in the MM layer and the substrate. The third column in Figure 3 shows a cross-sectional view of power loss density for the two resonance modes. For the lower frequency mode, most of the power is dissipated in the MM layer, while part of the power is dissipated in the substrate even though the MM layer absorbs the majority of the power for the higher frequency mode. In short, the broadband absorption results from the two resonance modes where both the MM layer and silicon substrate contribute to the absorption of the incident energy.

Photoexcitation of the All-Dielectric MPA. We have also investigated the tunable response of the all-dielectric MPA under optical excitation using optical-pump THz-probe (OPTP) spectroscopy.[31] For our experiment, the THz beam is at a 30° angle of incidence and the optical pump beam is normally incident. The pump beam is 800 nm near-infrared light with pulse duration of 35 fs, which arrives the sample 10 ps prior to the THz probe beam to ensure quasi-equilibrium of the electrons excited into the conduction band.

Figure 4a shows the OPTP spectra of the all-dielectric MPA. When there is no pump beam, the spectrum is similar to the THz-TDS measurement results shown in Figure 2d, even though the probe beam is obliquely incident (which can be verified by simulation results presented in Figure S6 of the Supporting Information). The peak absorption frequency is approximately 1.04 THz with bandwidth of 770 GHz, slightly different from the result for normal incidence. As the fluence of the pump beam increases to 4000 μJ/cm^2, the peak absorption frequency blueshift to 1.48 THz due to photoexcitation of carriers in silicon. At the same time, the bandwidth of 90% absorption decreases to 600 GHz and the peak absorption decreases from 99.6% to 97.2%, as illustrated in Figure 4b. When the fluence is higher than 400 μJ/cm^2, weak resonances arise at 0.45 THz and 0.92 THz, indicating new modes are present in the pumped condition. The absorbance at 0.5 THz is modulated from 80% to 36%.

It is interesting that additional resonance modes emerge under high optical pump fluence. In order to understand the

DOI: 10.1021/acsphotonics.8b01644
ACS Photonics 2019, 6, 830−837

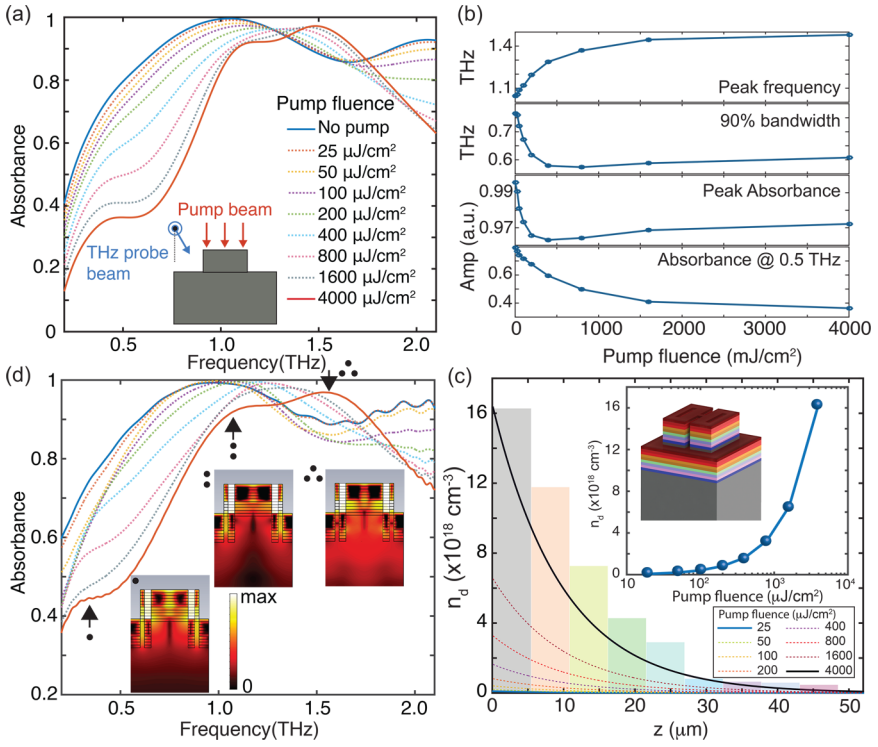

Figure 4. (a) OPTP spectra of the all-dielectric MPA for different pump fluences. Inset: incident direction of the beams; the optical pump beam is at normal incidence and the THz probe beam is at 30° angle of incidence. (b) The peak absorption frequency, 90% bandwidth, peak absorbance amplitude and absorbance at 0.5 THz vs pump fluence. (c) The theoretically calculated carrier density distribution along the *z*-axis in the all-dielectric MPA for different pump fluences. The bar plot represents the carrier density for each slice used in the simulation to match the spectrum for the maximum pump fluence. Inset: the carrier density at the top surface of the silicon as a function of fluence. Graphic inset: the slice configuration used in the simulation to represent the gradient carrier density. (d) Simulation results with layered carrier density distribution to match the measured spectrum for different pump fluences in (a). Insets: the power loss density distribution for each resonant mode.

physics behind this phenomenon, we have analyzed the carrier dynamics induced by the optical pump and simulated the absorbance spectra to compare with the experimental results. We first considered a homogeneous increase in the carrier densities in the silicon (including the MM layer and substrate) induced by the optical excitation. However, the simulated results fail to capture the resonance peaks at 0.45 THz and 0.92 THz, indicating that modeling the carrier concentration as homogeneous is inaccurate. Therefore, we consider nonuniformity in the distribution of carrier density. According to the Beer–Lambert law, for the 800 nm pump beam, the fluence decays exponentially along the propagation direction, with $f(z) = f_0 e^{-\alpha z}$. In this equation, f_0 is the fluence at the top surface of the silicon structure ($z = 0$), α ($\approx$1020 cm^{-1}) is the absorption coefficient for the pump beam,[36] and z is the depth in the silicon. We assume that all of the absorbed photons are converted to carriers in the silicon. The carrier density distribution in silicon along z direction can be estimated by

$$n_d(z) = \frac{1}{E_{photon}} \cdot \frac{df(z)}{dz} = \frac{\alpha f_0 e^{-\alpha z}}{E_{photon}} \quad (5)$$

where E_{photon} ($= h\nu$) is the photon energy of the pump beam, h is Planck's constant, and ν is the frequency of the pump beam. The carrier density (n_d) distribution is shown in Figure 4c for different pump fluences, indicating that the maximum carrier density is achieved at the top surface and decays exponentially into the surface. The carrier density at the top surface of silicon is related linearly to the pump fluence, as shown in the inset of Figure 4c, and the maximum carrier density is approximately 16×10^{18} cm^{-3} for the maximum pump fluence (i.e., 4000 μJ/cm^2), which is of the same order as previously reported values.[31,36]

The analysis of carrier density distribution indicates that we are unable to excite the all-dielectric MPA structure homogeneously using the pump beam. The height of the MM layer is 53 μm, which necessitates a carrier density gradient to be considered in our simulations. However, it is difficult to include spatially distributed carrier densities in the numerical simulations. Therefore, we divide the MM layer into ten slices with each slice having a thickness of 5.3 μm, as shown in the inset of Figure 4c. The top of the substrate is also divided to ten slices with identical thickness (5.3 μm). We approximate the different carrier density in each slice to model the gradient distribution of the carrier density. For example, we set the top two layers with a carrier density of 0.1×10^{18} cm^{-3} but the other slices without any changes to fit the measured absorbance under 25 μJ/cm^2, as shown in Figure 4d. As the pump fluence increases, we observe that the absorbance spectrum shift is similar to the experimental results when we use the carrier density listed in Table S2 in the Supporting Information. When the pump fluence is higher than 800 μJ/cm^2, the simulation results with a gradient carrier density distribution match the experimental results well, indicated by the appearance of the resonance at 0.45 THz. For the highest pump fluence, the carrier density distribution in the simulation follows the theoretical carrier density gradient, as shown in Figure 4c, and the spectrum exhibits three resonance frequencies, agreeing with the experimental results. In Figure

DOI: 10.1021/acsphotonics.8b01644
ACS Photonics 2019, 6, 830–837

4c, a plot of the power loss density for each resonance frequency is shown. We can see that the power loss is low in the top layers that have a higher carrier density, and the majority of the power is dissipated in the bottom layers that have a lower carrier density. This may be a result of the high carrier density regions screening electromagnetic waves entirely whereas the low density regions allow the wave to propagate and dissipate. For intermediate pump fluences, the carrier densities used in the simulation also follow the theoretical gradient, as shown in Figure S7 in the Supporting Information. The agreement between simulation and experiment provides compelling evidence that the carrier density gradient induced by the pump modulates the absorbance of the all-dielectric MPA with three-dimensional unit cell structures.

This finding implies that the variations in the pump fluence along the vertical direction in the MMs induces a carrier density gradient, providing a route for versatile control or fine-tuning of the MM or MPA response. Indeed, in our all-dielectric MPA, the emergence of multiple resonance modes at high pump fluence results from the gradient of the carrier density distribution. It may be possible to control the response of MMs with large vertical dimension using a spatial gradient pump beam. For example, two pump beams would interfere along the vertical direction to form a grating-like carrier distribution in the MM layer to manipulate the MM response. By tuning the vertical grating-like interference pattern of the pump beam, it may be possible to modulate the MM response temporally and spatially, which could enable exploration of ideas such as nonreciprocal MMs that only allow unidirectional light (probe beam) propagation.[37]

CONCLUSION

We have reported an all-dielectric THz metamaterial perfect absorber exhibiting broadband absorption. We designed and fabricated a metamaterial structure on doped silicon substrate to form the MPA. Near 100% absorbance is achieved at 1.0 THz and the 90% absorbance bandwidth is approximately 914 GHz for normal incidence. We utilized effective medium theory to interpret the perfect absorption response qualitatively, providing a general analytical tool to design and optimize all-dielectric perfect absorbers. The all-dielectric MPA is directly etched using a doped silicon substrate, which is compatible with CMOS-based THz detectors. Moreover, the dynamic response of the MPA has been investigated under optical pump beam excitation. In order to fit the experimental results, we have analyzed the carrier density distribution induced by the pump light absorption in the three-dimensional MM structure and included this gradient in our numerical simulations. The agreement between simulation and measured results indicates that the carriers are not uniformly distributed in the 3D MM structure, but varies with the penetration depth of the pump light. In summary, we present a broadband all-dielectric MPA with an optically tunable response that can be applied to constructing CMOS-compatible devices for THz sensing and imaging applications.

METHODS

Simulation of the All-Dielectric MPA. The finite different time domain (FDTD) solver, CST Microwave Studio, is used to simulate the response of the all-dielectric MPA. In the simulation, periodic boundary conditions are employed in conjunction with waveguide ports. The silicon is modeled with a Drude response, that is, $\varepsilon_{Si}(\omega) = \varepsilon_\infty - \omega_p^2/(\omega^2 + j\omega\Gamma)$, where ε_∞ (=11.68) is the high-frequency permittivity of silicon, ω_p is the plasma frequency and Γ is the collision frequency. The plasma frequency (ω_p) is given by $\omega_p = \sqrt{n_d e^2/(\varepsilon_0 m^*)}$, where n_d is the carrier density, e is the charge of an electron, ε_0 is the permittivity of free space, and m^* (= $0.37m_0$, m_0: the mass of an electron) is the effective mass of the carriers in silicon. The collision frequency is given by $\Gamma = \mu m^*/e$, where μ (= 386 $cm^2\ V^{-1}\ s^{-1}$) is the mobility of carriers based on empirical results.[38] For the original unpumped state, the carrier density is approximately 0.03×10^{18} cm^{-3}, obtained from the nominal DC conductivity of the silicon wafer.[39] Under optical pump excitation, carriers are excited in silicon and the carrier density gradient is generated in the structure, as shown in Figure 4. We neglect changes in the mobility and effective mass to simplify the modeling.

Effective Parameter Extraction of the Metamaterials. In order to extract the effective properties of the metamaterial layer, we first simulated the metamaterial layer without the substrate in a vacuum environment to obtain the reflection and transmission coefficient parameters, that is, S-parameters. Then, we converted the S-parameters to a transfer matrix and de-embedded the MM response from the overall response.[33] Finally, we calculated the effective parameters, including the permittivity and permeability, using the formulas described in.[33,34] We verified the extracted parameters by applying them to the transfer matrix model as illustrated in eqs 1 and 2 to calculate the extracted spectrum, which agrees well with the FDTD results.

Fabrication of the All-Dielectric MPA. The all-dielectric MPA was fabricated from a commercially available p-type doped silicon wafer (300 μm thick) using conventional photolithography and deep reactive-ion etching (DRIE) based on large-scale microfabrication techniques. A 5 μm thick layer of photoresist (AZ9260, Microchemicals GmbH) was spin coated on top of the wafer followed by photolithography (MA6, Suss Microtec Group) to achieve the pattern of the microstructure. Then DRIE (Surface Technology Systems) was employed to etch the "H-shaped" unit cell arrays on the substrate to desired depth. The DRIE process was implemented via the Bosch process, in which SF_6 was employed as the etching gas and CF_4 was the passivation gas. There were 60 cycles in total to etch the designed pattern down to the desired thickness. Each cycle includes 8s for etching and 4s for passivation. The wafer was cleaned with acetone to remove the photoresist after DRIE. Afterward, the depth of the sample was measured with surface profiler. The total size of a sample is 1.0×1.0 cm^2, including $\sim 71 \times 71$ unit cells.

Characterization of the All-Dielectric MPA. The static response of the all-dielectric MPA was characterized using THz time domain spectroscopy (TDS) based on photoconductive antennas, as shown in Figure S8a in the Supporting Information. A near-infrared (800 nm) Ti:sapphire laser with pulse duration of 25 fs and repetition rate of 80 MHz illuminates a biased photoconductive antenna to generate THz pulses. The THz pulses were focused on our MPA sample through a set of parabolic mirrors and the transmitted and reflected pulses were measured by another photoconductive antenna. In the measurement, the electric field was polarized perpendicular to the side bars of the H-shaped unit cell, that is, along the x-axis, as shown in Figure 1a. We obtained the

DOI: 10.1021/acsphotonics.8b01644
ACS Photonics 2019, 6, 830−837

temporal response of the sample, which is converted to frequency spectrum via Fourier transform. A gold mirror was used as a reference for the measurement of reflection response. The experiments were performed in a dry air chamber in order to avoid the THz radiation absorption of the water vapor. In the optical pump THz probe (OPTP) spectroscopy to measure the dynamic response of the all-dielectric MPA, the 800 nm optical pump beam was incident normally and the probe beam is 30° obliquely incident to the sample, as shown in Figure S8b in the Supporting Information.

■ ASSOCIATED CONTENT

Supporting Information

The Supporting Information is available free of charge on the ACS Publications website at DOI: 10.1021/acsphotonics.8b01644.

Supporting figures and details of the simulation, characterization, and result analyses (PDF).

■ AUTHOR INFORMATION

Corresponding Authors

*E-mail: raveritt@ucsd.edu.
*E-mail: xinz@bu.edu.

ORCID

Yue Wang: 0000-0003-2232-2783
Xin Zhang: 0000-0002-4413-5084

Author Contributions

†These authors contributed equally.

Notes

The authors declare no competing financial interest.

■ ACKNOWLEDGMENTS

This work was supported by the National Science Foundation under ECCS-1810252 and by the Project of High Talent Level of Xi'an University of Technology. Terahertz measurements at UCSD performed under DOE-BES DE-SC0018218.

■ REFERENCES

(1) Koenig, S.; Lopez-Diaz, D.; Antes, J.; Boes, F.; Henneberger, R.; Leuther, A.; Tessmann, A.; Schmogrow, R.; Hillerkuss, D.; Palmer, R.; Zwick, T.; Koos, C.; Freude, W.; Ambacher, O.; Leuthold, J.; Kallfass, I. Wireless sub-THz communication system with high data rate. *Nat. Photonics* **2013**, *7*, 977−981.

(2) Kurt, H.; Citrin, D. S. Photonic crystals for biochemical sensing in the terahertz region. *Appl. Phys. Lett.* **2005**, *87*, No. 041108.

(3) Fan, S.; Li, T.; Zhou, J.; Liu, X.; Liu, X.; Qi, H.; Mu, Z. Terahertz non-destructive imaging of cracks and cracking in structures of cement based materials. *AIP Adv.* **2017**, *7*, 115202.

(4) Chen, H.-T.; Padilla, W. J.; Cich, M. J.; Azad, A. K.; Averitt, R. D.; Taylor, A. J. A metamaterial solid-state terahertz phase modulator. *Nat. Photonics* **2009**, *3*, 148−151.

(5) Watts, C. M.; Liu, X.; Padilla, W. J. Metamaterial electromagnetic wave absorbers. *Adv. Mater.* **2012**, *24*, OP98−OP120.

(6) Tao, H.; Landy, N. I.; Bingham, C. M.; Zhang, X.; Averitt, R. D.; Padilla, W. J. A metamaterial absorber for the terahertz regime: Design, fabrication and characterization. *Opt. Express* **2008**, *16*, 7181−7188.

(7) Chen, H.-T. Interference theory of metamaterial perfect absorbers. *Opt. Express* **2012**, *20*, 7165−7172.

(8) Duan, G.; Schalch, J.; Zhao, X.; Zhang, J.; Averitt, R. D.; Zhang, X. Identifying the perfect absorption of metamaterials absorbers. *Phys. Rev. B: Condens. Matter Mater. Phys.* **2018**, *97*, No. 035128.

(9) Wen, Q.-Y.; Zhang, H.-W.; Xie, Y.-S.; Yang, Q.-H.; Liu, Y.-L. Dual band terahertz metamaterial absorber: Design, fabrication, and characterization. *Appl. Phys. Lett.* **2009**, *95*, 241111.

(10) Shen, X.; Yang, Y.; Zang, Y.; Gu, J.; Han, J.; Zhang, W.; Cui, T. J. Triple-band terahertz metamaterial absorber: Design, experiment, and physical interpretation. *Appl. Phys. Lett.* **2012**, *101*, 154102.

(11) Li, Y.; An, B.; Jiang, S.; Gao, J.; Chen, Y.; Pan, S. Plasmonic induced triple-band absorber for sensor application. *Opt. Express* **2015**, *23*, 17607−17612.

(12) Withayachumnankul, W.; Shah, C. M.; Fumeaux, C.; Ung, B. S.-Y.; Padilla, W. J.; Bhaskaran, M.; Abbott, D.; Sriram, S. Plasmonic resonance toward terahertz perfect absorbers. *ACS Photonics* **2014**, *1*, 625−630.

(13) Liu, X.; Fan, K.; Shadrivov, I.; Padilla, W. J. Experimental realization of a terahertz all-dielectric metasurface absorber. *Opt. Express* **2017**, *25*, 191−201.

(14) Wu, M.; Zhao, X.; Zhang, J.; Schalch, J.; Duan, G.; Cremin, K.; Averitt, R. D.; Zhang, X. A three-dimensional all-metal terahertz metamaterial perfect absorber. *Appl. Phys. Lett.* **2017**, *111*, No. 051101.

(15) Zhao, X.; Fan, K.; Zhang, J.; Seren, H. R.; Metcalfe, G. D.; Wraback, M.; Averitt, R. D.; Zhang, X. Optically tunable metamaterial perfect absorber on highly flexible substrate. *Sens. Actuators, A* **2015**, *231*, 74−80.

(16) Seren, H. R.; Keiser, G. R.; Cao, L.; Zhang, J.; Strikwerda, A. C.; Fan, K.; Metcalfe, G. D.; Wraback, M.; Zhang, X.; Averitt, R. D. Optically modulated multiband terahertz perfect absorber. *Adv. Opt. Mater.* **2014**, *2*, 1221−1226.

(17) Miao, Z.; Wu, Q.; Li, X.; He, Q.; Ding, K.; An, Z.; Zhang, Y.; Zhou, L. Widely tunable terahertz phase modulation with gate-controlled graphene metasurfaces. *Phys. Rev. X* **2015**, *5*, No. 041027.

(18) Cui, Y.; Fung, K. H.; Xu, J.; Ma, H.; Jin, Y.; He, S.; Fang, N. X. Ultrabroadband light absorption by a sawtooth anisotropic metamaterial slab. *Nano Lett.* **2012**, *12*, 1443−1447.

(19) Zhu, J.; Ma, Z.; Sun, W.; Ding, F.; He, Q.; Zhou, L.; Ma, Y. Ultra-broadband terahertz metamaterial absorber. *Appl. Phys. Lett.* **2014**, *105*, No. 021102.

(20) Moitra, P.; Slovick, B. A.; Gang Yu, Z.; Krishnamurthy, S.; Valentine, J. Experimental demonstration of a broadband all-dielectric metamaterial perfect reflector. *Appl. Phys. Lett.* **2014**, *104*, 171102.

(21) Sheng, Y.; Zhu, J.; Xu, W.; Jiang, W.; Yuan, J.; Yin, G.; Xie, L.; Ying, Y.; Ma, Y. High-performance terahertz wave absorbers made of silicon-based metamaterials. *Appl. Phys. Lett.* **2015**, *107*, No. 073903.

(22) Zang, X.; Shi, C.; Chen, L.; Cai, B.; Zhu, Y.; Zhuang, S. Ultra-broadband terahertz absorption by exciting the orthogonal diffraction in dumbbell-shaped gratings. *Sci. Rep.* **2015**, *5*, 8901.

(23) Peng, Y.; Zang, X.; Zhu, Y. M.; Shi, C.; Chen, L.; Cai, B.; Zhuang, S. Ultra-broadband terahertz perfect absorber by exciting multi-order diffractions in a double-layered grating structure. *Opt. Express* **2015**, *23*, 2032−2039.

(24) Kakimi, R.; Fujita, M.; Nagai, M.; Ashida, M.; Nagatsuma, T. Capture of a terahertz wave in a photonic crystal slab. *Nat. Photonics* **2014**, *8*, 657−663.

(25) Ling, X.; Xiao, Z.; Zheng, X.; Tang, J.; Xu, K. A three-dimensional ultra-broadband metamaterial absorber in terahertz region. *Appl. Phys. A: Mater. Sci. Process.* **2016**, *122*, 951.

(26) Gorgulu, K.; Yilmaz, M.; Topalli, K.; Okyay, A. K. Wideband 'black silicon' for mid-infrared applications. *J. Opt.* **2017**, *19*, No. 065101.

(27) Gorgulu, K.; Gok, A.; Yilmaz, M.; Topalli, K.; Okyay, A. K. High-conductivity silicon based spectrally selective plasmonic surfaces for sensing in the infrared region. *J. Opt.* **2017**, *19*, No. 025002.

(28) Gorgulu, K.; Gok, A.; Yilmaz, M.; Topalli, K.; Biyiki, N.; Okyay, A. K. All-Silicon Ultra-Broadband Infrared Light Absorbers. *Sci. Rep.* **2016**, *6*, 38589.

(29) Gok, A.; Yilmaz, M.; Biyikli, N.; Topalli, K.; Okyay, A. K. Practical multi-featured perfect absorber utilizing high conductivity silicon. *J. Opt.* **2016**, *18*, No. 035002.

DOI: 10.1021/acsphotonics.8b01644
ACS Photonics 2019, 6, 830−837

(30) Seren, H. R.; Zhang, J.; Keiser, G. R.; Maddox, S. J.; Zhao, X.; Fan, K.; Bank, S. R.; Zhang, X.; Averitt, R. D. Nonlinear terahertz devices utilizing semiconducting plasmonic metamaterials. *Light: Sci. Appl.* **2016**, *5*, No. e16078.
(31) Fan, K.; Zhang, J.; Liu, X.; Zhang, G.-F.; Averitt, R. D.; Padilla, W. J. Phototunable dielectric Huygens' metasurfaces. *Adv. Mater.* **2018**, *30*, 1800278.
(32) Smith, D. R.; Vier, D. C.; Koschny, T.; Soukoulis, C. M. Electromagnetic parameter retrieval from inhomogeneous metamaterials. *Phys. Rev. E* **2005**, *71*, No. 036617.
(33) Kriegler, C. E.; Rill, M. S.; Linden, S.; Wegener, M. Bianisotropic Photonic Metamaterials. *IEEE J. Sel. Top. Quantum Electron.* **2010**, *16*, 367−375.
(34) Byrnes, S. J. Multilayer optical calculations. *arXiv:1603.02720,* **2016**, na.
(35) Kapoor, A.; Singh, G. S. Mode classification in cylindrical dielectric waveguides. *J. Lightwave Technol.* **2000**, *18*, 849−852.
(36) Sabbah, A. J.; Riffe, D. M. Femtosecond pump-probe reflectivity study of silicon carrier dynamics. *Phys. Rev. B: Condens. Matter Mater. Phys.* **2002**, *66*, 165217.
(37) Feng, L.; Xu, Y.-L.; Fegadolli, W. S.; Lu, M.-H.; Oliveira, J. E. B.; Almeida, V. R.; Chen, Y.-F.; Scherer, A. Experimental demonstration of a unidirectional reflectionless parity-time metamaterial at optical frequencies. *Nat. Mater.* **2013**, *12*, 108−113.
(38) Neamen, D. *Semiconductor Physics and Devices*; McGraw-Hill: New York, 2003.
(39) Thurber, W. R.; Mattis, R. L.; Liu, Y. M.; Filliben, J. J. Resistivity-dopant density relationship for boron doped silicon. *J. Electrochem. Soc.* **1980**, *127*, 2291−2294.

DOI: 10.1021/acsphotonics.8b01644
ACS Photonics 2019, 6, 830−837